The optimal windows for seismically-enhanced gold precipitation in the epithermal environment

Pablo Sanchez-Alfaro [a,b,*,1], Martin Reich [a,b], Thomas Driesner [c], José Cembrano [b,d], Gloria Arancibia [b,d], Pamela Pérez-Flores [b,d], Christoph A. Heinrich [c], Julie Rowland [e], Daniele Tardani [a,b], Dietrich Lange [f], Eduardo Campos [g]

[a] Department of Geology, Universidad de Chile, 8370450 Santiago, Chile
[b] Andean Geothermal Center of Excellence (CEGA), Universidad de Chile, Santiago, Chile
[c] Department of Earth Sciences, Swiss Federal Institute of Technology, ETH Zentrum NO, 8092 Zürich, Switzerland
[d] Department of Structural and Geotechnical Engineering, Pontificia Universidad Católica de Chile, 7820436 Santiago, Chile
[e] School of Environment, The University of Auckland, Auckland, New Zealand
[f] GEOMAR, Helmholtz-Zentrum für Ozeanforschung Kiel, Kiel, Germany
[g] Departamento de Ciencias Geológicas, Universidad Católica del Norte, Antofagasta, Chile

ARTICLE INFO

ABSTRACT

Epithermal gold (Au) deposits result from the combination of a sustained flux of metal-rich fluids and an efficient precipitation mechanism. Earthquakes may trigger gold precipitation by rapid loss of fluid pressure but their efficiency and time-integrated contribution to gold endowment are poorly constrained. In order to quantify the feedbacks between earthquake-driven fracturing and gold precipitation in the shallow crust, we studied the gold-rich fluids in the active Tolhuaca geothermal system, located in the highly seismic Southern Andes of Chile. We combined temperature measurements in the deep wells with fluid inclusion data, geochemical analyses of borehole fluids and numerical simulations of coupled heat and fluid flow to reconstruct the physical and chemical evolution of the hydrothermal reservoir. The effect of seismic perturbations on fluid parameters was constrained using a thermo-mechanical piston model that simulates the suction pump mechanism occurring in dilational jogs. Furthermore, we evaluated the impact of fluid parameters on gold precipitation by calculating the solubility of gold in pressure (P)–enthalpy (H) space. The reconstructed fluid conditions at Tolhuaca indicate that single-phase convective fluids feeding the hydrothermal reservoir reach the two-phase boundary with a high gold budget (~1–5 ppb) at saturated liquid pressures between 20 and 100 bar (210 °C < T_{sat} < 310 °C). We show that if hydrothermal fluids reach this optimal threshold for gold precipitation at a temperature near 250 °C, small adiabatic pressure drops (~10 bar) triggered by transient fault-rupture can produce precipitation of 95% of the dissolved gold. Our results at the active Tolhuaca geothermal system indicate that subtle, externally-forced perturbations – equivalent to low magnitude earthquakes (Mw < 2) of a hydrothermal reservoir under optimal conditions – may significantly enhance gold precipitation rates in the shallow crust and lead to overall increases in metal endowment over time.

© 2016 Elsevier B.V. All rights reserved.

1. Introduction

The interplay between seismic activity, fluid flow and mineral precipitation exerts a first-order control on the strength and permeability of the crust, and plays a critical role in promoting the development of hydrothermal systems and the formation of giant ore deposits (Richards, 2013; Sibson, 1987). External forcing such as earthquakes can have a profound impact on metal solubility, triggering physical and chemical changes in ore fluids that can enhance the precipitation process by phase separation (Rowland and Simmons, 2012; Sibson et al., 1988). This is particularly relevant in shallow crustal settings where porphyry copper and epithermal gold deposits form as a result of phase separation or boiling of a single-phase fluid. In the epithermal environment, in particular, precipitation of gold and/or silver may occur in association with gentle boiling, where fluid enthalpy is sufficiently high to produce a small vapor fraction upon ascent, or with flash vaporization forced by a transient pressure drop that converts most of the original liquid into a low density vapor phase (Moncada et al., 2012;

* Corresponding author at: Department of Geology, Universidad de Chile, 8370450 Santiago, Chile.
E-mail address: vsanchez@ing.uchile.cl (P. Sanchez-Alfaro).
[1] Present address: School of Environment, The University of Auckland, Auckland, New Zealand.

Simmons et al., 2005; Weatherley and Henley, 2013). There is abundant evidence in the literature documenting that both permeability and gold precipitation are strongly affected by pressure changes triggered by earthquakes (Rowland and Simmons, 2012; Sibson et al., 1988; Weatherley and Henley, 2013). Furthermore, studies have inferred that flash vaporization of gold-rich fluids in dilational jogs during an earthquake can result in the rapid co-deposition of silica to form gold-enriched quartz veins (Moncada et al., 2012; Sibson, 1987; Weatherley and Henley, 2013). However, these concepts have never been tested for the effect of externally-triggered pressure variations on gold solubility in the epithermal environment. Therefore, the relative contribution of seismic activity on gold precipitation rates – and thus, on the overall metal endowment of epithermal gold deposits – remains largely unknown.

In this study, we integrate geochemical data of gold-bearing borehole fluids with temperature profiles in an active, high-enthalpy geothermal system at Tolhuaca, in the seismically active Chilean Southern Andes. By combining these data with thermodynamic calculations of gold solubility and simulations on pressure drops driven by earthquakes, we constrain the optimal depth window for seismically enhanced gold precipitation. Our analysis points to favorable conditions for highly efficient gold extraction from hydrothermal fluids by flash vaporization in the epithermal environment. We further quantify the magnitude of these externally triggered perturbations, and explore the role of frequent, low-magnitude seismic activity as a relevant factor in building epithermal gold deposits in tectonically active regions.

2. Geological setting

The Andean Cordillera of Central-Southern Chile, where hydrothermal systems occur in close spatial relationship with active volcanism as well as major seismically-active fault systems, provides an excellent natural laboratory to study the interplay between earthquakes, fluid flow and metal precipitation (Fig. 1). In this region it has been shown that the nature and evolution of volcanic and hydrothermal systems is controlled by the NNE-striking, 1200 km long Liquiñe–Ofqui Fault System (LOFS) and the NW-striking Arc-Oblique Fault System (ALFS) (Cembrano and Lara, 2009; Sánchez et al., 2013; Tardani et al., 2016; Perez-Flores et al., 2016). Within this setting, the active Tolhuaca geothermal field in the northern termination of the LOFS hosts a high enthalpy system that has been drilled to ~3 km depth, but is not yet affected by geothermal production or re-injection (Melosh et al., 2012; Sánchez et al., 2016).

Geological mapping, drillcore logging studies and kinematic analysis of fault-slip data have revealed that the Tolhuaca geothermal system is characterized by a structural and mineralogical compartmentalization in a transtensional stress regime (Sanchez-Alfaro et al., 2016). Based on core logging, mineralogical observations and fluid inclusion data, four stages (S1–S4) of progressive hydrothermal alteration have been recognized (Sanchez-Alfaro et al., 2016). An early heating event (S1) was followed by the formation of a clay-rich cap in the upper zone (<670 m) and the development of a propylitic alteration assemblage at greater depth (S2). Boiling, flashing and brecciation occurred later (S3), followed by a final phase of fluid mixing and boiling (S4). The ubiquitous co-precipitation of silica phases (amorphous silica, chalcedony and quartz) and the formation of hydrothermal breccias at the end of S1 are indicative of widespread boiling and flashing conditions (Sanchez-Alfaro et al., 2016). Calcite with lattice-bladed texture, quartz with plumose texture and the coexistence of silica phases with variable degrees of crystallinity formed in stage S3, are indicative of boiling and flashing episodes which are likely triggered by transient pressure drops during the hydrothermal evolution at Tolhuaca (Sanchez-Alfaro et al., 2016). Transient pressure changes triggered by seismicity are likely produced at the tip of faults and in linkage zones, such as dilational jogs (Curewitz and Karson, 1997; Sibson, 1987; Weatherley and Henley,

2013). At Tolhuaca, structural logging of the Tol-1 core indicates the presence of dilational jogs infilled with calcite and quartz (Fig. 1 D&E; Sanchez-Alfaro et al., 2016). In the vicinities of Tolhuaca volcano, detailed structural studies of fault systems revealed that dilatational jogs are formed at linking zones between NNE- and NE-striking faults. Syntaxial bladed-like calcite crystals of about 1 cm in size fill these dilatational jogs which indicate transient pressure drop likely related to fault activity in the LOFS (Perez-Flores et al., 2016). Therefore, the Tolhuaca geothermal system is a good analogue to evaluate the impacts of internal and external triggers on fluid evolution and mineralization in a hydrothermal reservoir.

3. Methods

Considering the role of phase separation in the precipitation of precious minerals in the epithermal environment, we use pressure–enthalpy (P–H) space to represent the thermodynamic conditions of the system. The P–H space allows the visualization of vapor fractions in the two-phase region, reduced to a line in pressure–enthalpy space, and an intuitive representation of adiabatic (isoenthalpic) processes. This is justified because transient co-seismic thermodynamic changes are likely to be adiabatic in nature (Henley and Hughes, 2000).

In order to represent temperature logs of deep wells and homogenization temperatures of fluid inclusion data in P–H space, enthalpy was calculated as a function of temperature assuming liquid phase conditions and depth was converted to pressure assuming a hydrostatic gradient, as indicated by the temperature and pressure data from deep wells (Sánchez et al., 2016).

### 3.1. Gold solubility calculations in pressure–enthalpy space

The GEMS geochemical modeling software (Kulik et al., 2012) was used to compute dissolved gold concentration in hydrothermal fluids under epithermal conditions. As the gold solubility calculation is highly dependent on fluid chemistry (especially on sulfur content, salinity and pH), an accurate reconstruction of the chemical conditions of the deep reservoir is fundamental. Reservoir fluid samples are commonly collected at the wellhead after fluid ascent in the well has triggered depressurization boiling and separation between vapor and liquid. To reconstruct fluid chemistry at pre-sampling conditions the methodology developed by Scott et al. (2014) was used. Such methodology corrects the effect of the separation and segregation of liquid and vapor phases driven by adhesion of the liquid phase onto mineral surfaces in the porous aquifer rock upon rapid depressurization and boiling. The reconstruction was performed using the WATCH geochemical modeling software (Arnórsson et al., 1982), assuming a unique segregation step and using temperature measurements to constrain reservoir temperature. The reconstructed chemistry was obtained for major elements included in the thermodynamic database of WATCH, which are: SiO_2, B, Na, K, Ca, Mg, Al, Fe, CO_2, H_2S, SO_4, Cl and F. Volatiles such as CO_2 and H_2S are significantly affected by phase segregation whereas the non-volatile components such as Na, Cl and Si are only mildly affected.

For gold solubility calculations, feldspar-buffered acid-base conditions were assumed, i.e., excess Kfeldspar + albite + muscovite + quartz (Heinrich, 2005). The GEMS code uses the PSI/Nagra database (Hummel et al., 2002) as the core thermodynamic data source, which is complemented with SUPCRT92 (Johnson et al., 1992) for aqueous species and minerals. We updated the gold thermodynamic data for $Au(Cl)_n$, $Au(OH)_n$ and $Au(HS)_n$ species ($n = 1, 2$) with self-consistent experimental results (Stefánsson and Seward, 2004, 2003a, 2003b). Direct calculation of gold solubility with GEMS is restricted to the stability field of aqueous liquid, hereby computed within an equidistant temperature-pressure grid ($\Delta T = 5$ °C; $\Delta P = 10$ bar), ranging from 10 to 300 bar and 50–375 °C.
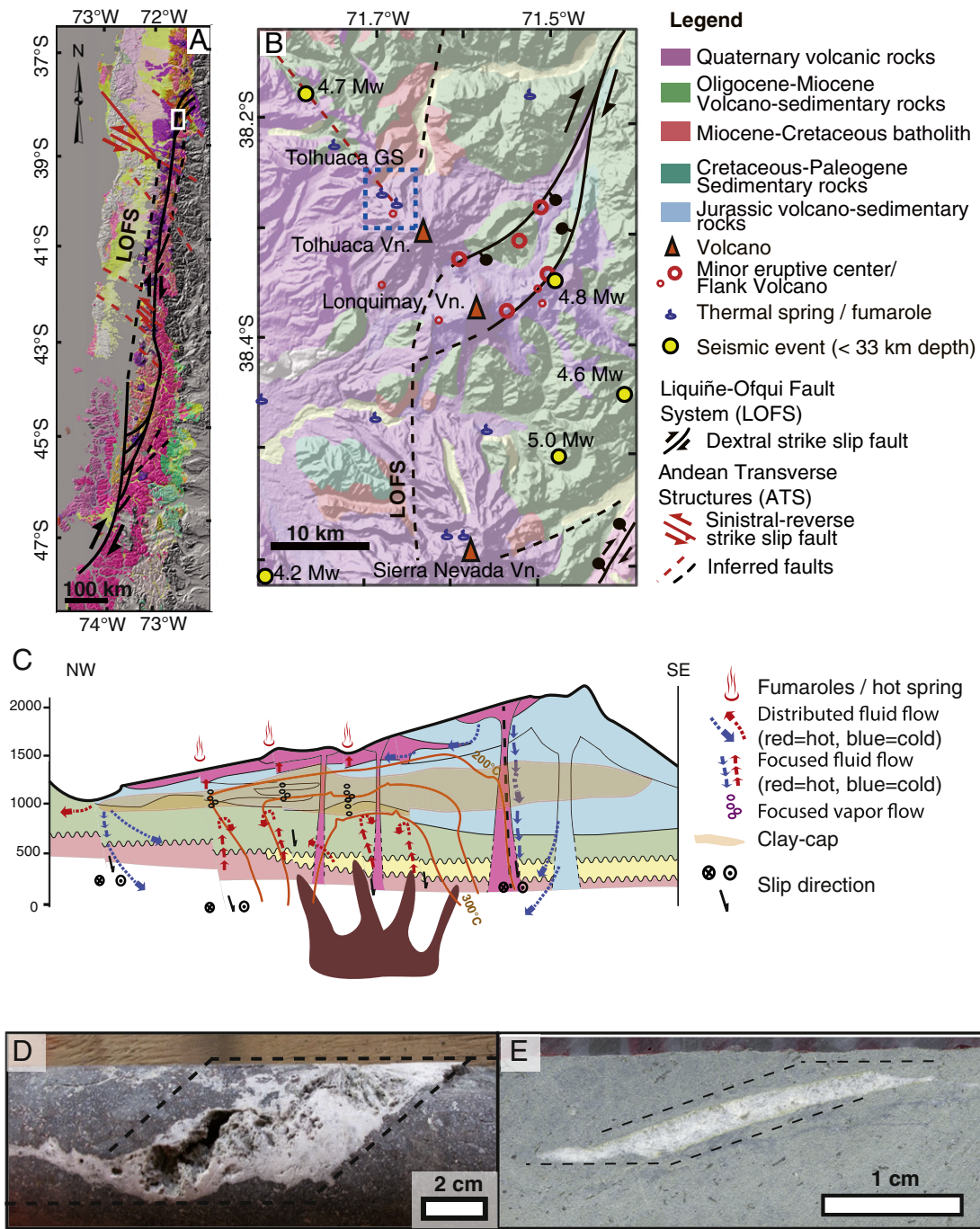
Fig. 1. Geodynamic and structural setting of the Tolhuaca geothermal system. (A) Digital elevation model showing the location and extent of the Liquiñe–Ofqui Fault System (LOFS; in black) and the Arc-Oblique Fault System (ALFS; in red) (Perez-Flores et al., 2016). (B) Simplified geological map showing the major structural systems in the studied area. Also, the spatial and genetic association between the LOFS and ALFS with the major stratovolcanoes, monogenetic cones and geothermal areas are shown (Perez-Flores et al., 2016). (C) Conceptual model of the Tolhuaca geothermal system at local scale showing the main hydrological features, modified from Sánchez et al. (2016). Photograph (D) and photomicrograph (E) of veins with the geometry of a dilational jog retrieved from the Tol-1 core. Vein in (D) is infilled by bladed calcite (minor quartz, chalcedony and iron oxides) whereas vein in (E) is infilled mainly by chalcedony (minor quartz, epidote, pyrite and wairakite).

In aqueous sulfide solutions gold dissolves according to the following reactions (1 & 2) (Stefánsson and Seward, 2004):

$$Au(s) + H_2S(aq) = AuHS(aq) + 0.5H_2(aq) \qquad (1)$$

$$Au(s) + H_2S(aq) + HS^- = Au(HS)_2^- + 0.5H_2(aq) \qquad (2)$$
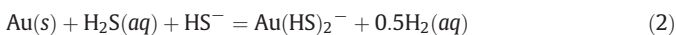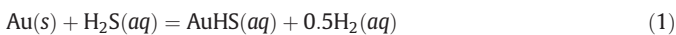
In epithermal environments, gold solubility is dominated by the $Au(HS)_2^-$ complex and therefore is strongly affected by the loss of sulfur in the two-phase region. To account for the effect of H_2S-loss, sulfur depletion was calculated using Henry's law. Then, the solubility of gold in the aqueous liquid was computed using GEMS for the S-depleted liquid fraction (m_{Au_liquid}) at saturated pressure ($P = P_{sat}$). Due to the low solvation capacity of low-density steam (Hurtig and Williams-Jones, 2014), it is reasonable to assume that the gold dissolved in the vapor is negligible. Therefore, the gold content at any point within the two-phase region was calculated as the gold dissolved in the liquid phase (m_{Au_liquid}) times the liquid mass fraction.

3.2. Gold precipitation efficiency and gold grades

The efficiency of gold precipitation from a hydrothermal fluid can be represented by the ratio of gold precipitated with respect to the initial gold content in the fluid, according to Eq. (3):

$$\text{Efficiency } [\%] = (m_{Au\_initial} - m_{Au\_final})/m_{Au\_initial} \qquad (3)$$

where m is the molality of Au in the initial fluid (at liquid saturated conditions of the reservoir) and final fluid (at any condition bellow critical pressure and temperature), as subscripted. We assume that the amount of gold precipitated is equivalent to the difference between initial and final gold solubility of the ore fluid.

The gold grade in idealized quartz veins was represented by the gold-quartz mass ratio resulting from the precipitation of a certain mass of fluid and calculated in mg of gold per kg of quartz. Quartz solubility in the liquid region was computed using the equation of Manning (1994) and calculated within the two-phase region by assuming that silica is only contained in the liquid fraction. The efficiency and the resulting gold grade of an idealized vein were computed for an adiabatic pressure drop and isobaric cooling mechanisms.

The thermodynamic properties of water and steam – such as P, T, H, ρ (density) and vapor fraction – were calculated in $P–H$ space using the freeware Matlab code XSteam (Holmgren, 2007), which implements the IAPWS IF-97 databases for the properties of water.

3.3. Suction-pump modeling

Ore bodies in epithermal gold deposits are commonly related to specific structural elements such as dilational jogs, fault step-overs and releasing bends (Rowland and Simmons, 2012; Sibson, 1987; Simmons et al., 2005). Co-seismic slip in these structural contexts causes transient changes in the physical and chemical conditions of hydrothermal fluids and triggers the precipitation of precious metals (Moncada et al., 2012; Sibson, 1987).

Therefore, in order to analyze the effect of earthquakes on gold solubility in the epithermal environment we constrained the co-seismic changes on fluid parameters within a dilational jog. We used the suction pump piston model from Weatherley and Henley (2013) to estimate the co-seismic pressure drop in a fault step-over. In the suction pump mechanism, pressure drop is driven by transient volume increase in the dilational jog or fault step-over as described in Fig. 2 (Sibson, 1987). The pressure drop produces the vaporization of most of the fluid within the dilational jog promoting the inflow of new hydrothermal fluid transported through the active fault and fracture networks (Weatherley and Henley, 2013).

The change in volume within a fault jog due to the action of an earthquake of certain magnitude can be calculated using well-established earthquake fault scaling relationships between fault width and length, co-seismic slip and earthquake magnitude (Leonard, 2014).

In the updated empirical scaling relations for strike-slip earthquakes from Leonard (2014), the rupture length (L) is given by:

$$\log_{10} L = \frac{M_w + 10.7 \times 1.5 - 14.862}{2.5} \qquad (4)$$

the average slip (s) is:

$$\log_{10} s = 0.833 \log_{10} L - 3.84 \qquad (5)$$

and width (W) of the rupture is: $W = L$ for small magnitude earthquakes (Mw < 5); $W = 15 * L^{2/3}$ for moderate earthquakes (5 < Mw < 6.5); $W = 17$ km, the mean crustal seismogenic width for large earthquakes (Mw > 6.5). Since we used an updated and corrected version of the earthquake scaling relations by Leonard (2014, 2012) the calculations are slightly different to those of Weatherley and Henley (2013) who used the scaling relations from Leonard (2010).

A Pre-rupture
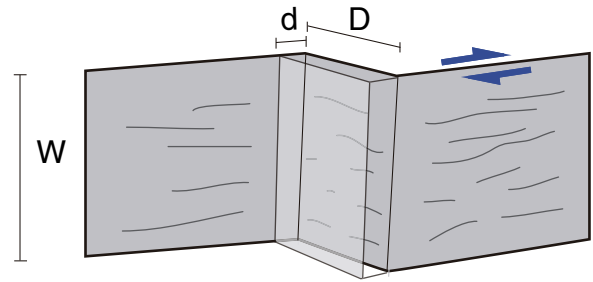
B Post-rupture
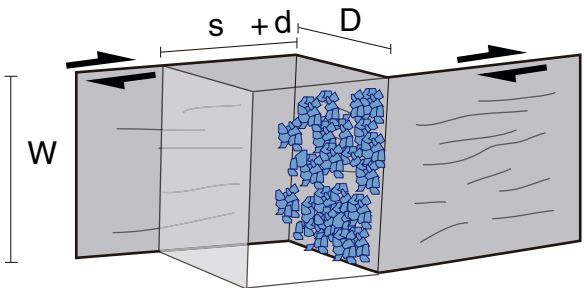
Fig. 2. Geometry of the suction pump model used to represent dilational jogs during faulting. (A) Pre-rupture conditions under a uniform fluid pressure regime. (B) Volume increase due to co-seismic slip causes flashing vaporization and solubility decrease of dissolved minerals. Fluid influx is enhanced from surrounding fault–fracture meshes. See details in the text.

The least constrained geometrical parameter in the model is the jog length (or step-over distance; D in Fig. 2) arbitrarily considered as 1 m. However, co-seismic pressure drop estimations are only dependent on the relative volume increase which is unaffected by variations on the jog length (D), as arises from the relative volume increase definition in Eq. (6):

$$\frac{V_i + \Delta V}{V_i} = 1 + \frac{s \times D \times W}{d \times D \times W} = 1 + \frac{s}{d} \qquad (6)$$

The initial effective aperture thickness of the dilational jog 'd' assumed for the model is 0.1 mm. This 'd' value is reasonable for representing a dilational jog with a restricted aperture just prior the co-seismic slip and/or the reactivation of a larger dilational jog that has been sealed by mineralization. However, our calculations would overestimate the pressure drop in the case of a dilational jog that is initially widely open (much higher 'd' values).

This model assumes that the fault jog is initially filled with fluid and that the transient boiling is adiabatic and sustained by heat transfer from wallrock to fluid, as a result of the decrease in temperature due to phase change (Henley and Hughes, 2000). By combining the relative volume changes with the thermodynamic properties of water, the transient fluid pressure and vapor fraction was computed for earthquakes of variable magnitude.

The fault-valve mechanism also may occur in hydrothermal systems, but unlike the suction pump, it is driven by pore fluid overpressure (Sibson et al., 1988). This mechanism is generally considered in the context of orogenic gold deposits, in which unfavorably oriented reverse faults are activated by substantial increases in fluid pressure, optimizing conditions for gold deposition across fault-valves (Sibson and Scott, 1998). However, hydraulic activation of brittle failure also exerts a profound influence on fluid migration in epithermal environments, which typically are associated with extensional (transtensional) tectonics (Sillitoe and Hedenquist, 2003). In these settings, very small increases in pressure may result in fluid flow through mixed-mode meshes of

faults and fractures (Sibson, 2003), perhaps explaining the prevalence of seismic swarm activity in active environments (Rowland and Simmons, 2012; Sibson, 2003; Sibson et al., 1988). However, although we consider fault-valve behavior important at all scales in all tectonically active fluid regimes, we focus on the analysis of the suction pump mechanism because of its geometrical simplicity for demonstrating the effect of seismically-triggered pressure drops on gold precipitation.

4. Results

4.1. Thermodynamic conditions at Tolhuaca in pressure–enthalpy space

Major-element fluid chemistry of geothermal fluid was reconstructed at reservoir conditions following the phase segregation methods and used as the main input for gold solubility calculations (see Section 2.3). The concentration of major components estimated at reservoir conditions (P_{sat} = 85 bar) is Cl = 193, H_2S = 19.7, SO_4 = 6.3, Na = 131, K = 24, Al = 0.76, and SiO_2 = 364, in mg/kg of water. Metal content is indicated in Fig. 3 by the measured concentrations of trace elements including Au (1.6 µg/kg), Ag (0.018 µg/kg), Cu (0.07 µg/kg) and Zn (7.5 µg/kg).
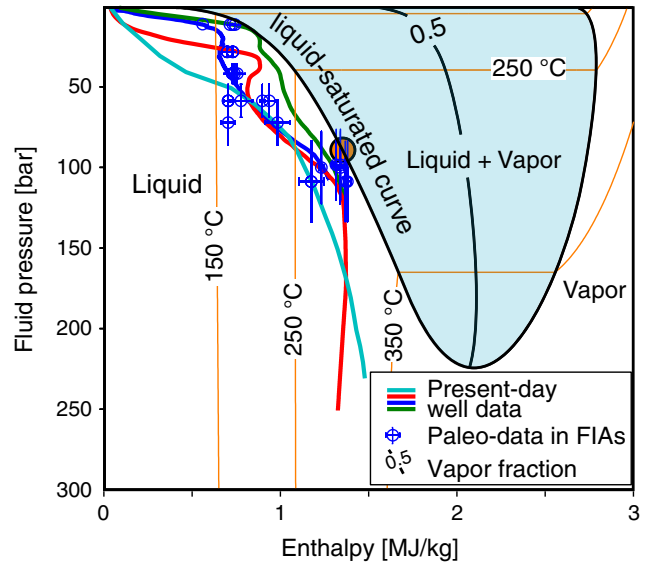
Present-day pressure and enthalpy conditions, calculated from temperature measurements in deep wells of the Tolhuaca geothermal system (Melosh et al., 2012; Sanchez-Alfaro et al., 2016) are shown in pressure–enthalpy (P–H) space in Fig. 4A. Additionally, measured homogenization temperatures of fluid inclusion assemblages hosted in quartz and calcite from Sanchez (2015) are used to estimate pressure and enthalpy and represent past conditions of the system in P–H space (Fig. 4B). Temperature, pressure and enthalpy data indicates that the geothermal reservoir reaches vapor saturated liquid at ~85 bar of pressure and ~300 °C of temperature.

4.2. Gold solubility in pressure–enthalpy space

To quantify the effect of the different fluid trajectories on the dissolved gold we calculated the solubility of gold in pressure–enthalpy
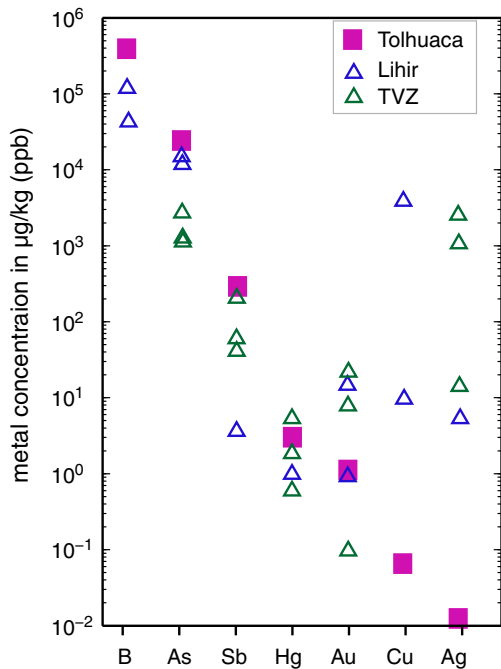
Fig. 4. Physicochemical evolution of the Tolhuaca hydrothermal system. Microthermometric data and present-day conditions in pressure–enthalpy (P–H) space. Blue open circles show the average homogenization temperatures of fluid inclusions with 1-sigma standard deviation. Depth was converted to pressure assuming a hydrostatic gradient, and vertical error bars indicate the difference between hydrostatic and boiling pressure gradient. The colored curves show the temperature profiles obtained in four boreholes at Tolhuaca. The orange circle shows the estimated reservoir conditions.
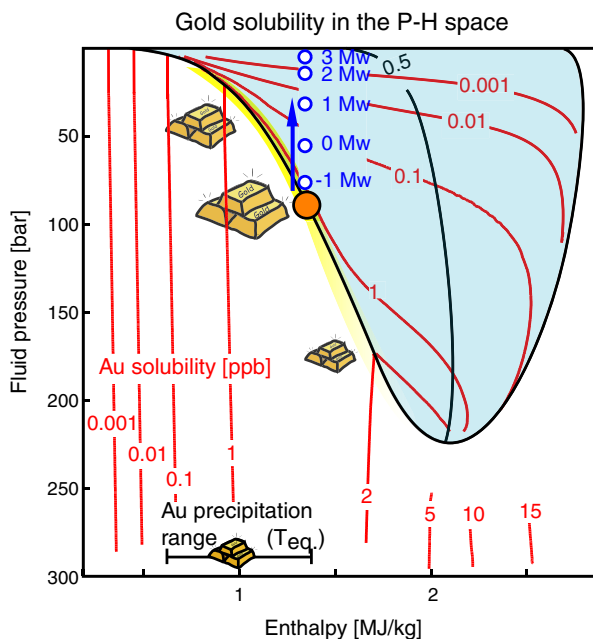
space, allowing a clear representation of adiabatic pressure changes. We used the reconstructed chemistry from the Tolhuaca fluid at the estimated reservoir conditions as a reasonable starting point for calculations.

In Fig. 5, the calculated isopleths (red lines) show high solubility conditions for gold in the liquid-phase region between ~210 and 370 °C (P_{sat} = 20 to 220 bar). For these conditions, the calculated isopleths indicate that a subtle adiabatic pressure drop of ~10 bar from liquid-saturated conditions (shaded in yellow), where saturated liquid pressure (P_{sat}) ranges between 20 and 100 bar (210 °C < T_{sat} < 310 °C), causes a sharp decrease in gold solubility (Fig. 5, blue vertical arrow). If the adiabatic pressure drop occurs at higher pressures ($P > P_{sat}$ ~ 100 bar), the solubility decrease is moderate.

Calculations of the efficiency of gold precipitation indicate that starting from the estimated Tolhuaca geothermal reservoir condition (T_{sat} ~ 300 °C, P_{sat} ~ 85 bar, orange circle in Fig. 6A) an adiabatic pressure drop of 10 bar produces the precipitation of >50% of the gold initially dissolved while a pressure drop of 20 bar precipitates near 70%. Starting from a lower enthalpy condition (T_{sat} ~ 250 °C, P_{sat} ~ 40 bar) an adiabatic pressure drop of 5 bar has a gold precipitation efficiency of 70% while a 10 bar pressure drop leads to a 95% efficiency. Conversely, if the fluid follows a cooling path and starts at reservoir conditions, it requires a temperature decrease of 100 °C for 50% efficiency and 160 °C for 95% efficiency.

Fig. 6B shows the gold solubility versus pressure for gentle boiling and adiabatic decompression paths. For the gentle boiling path – following the boiling curve – the gold solubility decrease is driven by the decrease of saturated-liquid temperature and is very sharp only at pressures bellow 15 bar (T_{sat} = ~200 °C). Contrastingly, the solubility drop in the adiabatic decompression path is produced mainly by H_2S loss and is significantly steeper than the gentle boiling path.

The quartz solubility data (Fig. 6C) allow calculating the gold–quartz mass ratio for idealized quartz veins (Fig. 6D), as a proxy for the gold grade resulting from cooling and adiabatic decompression paths. The estimated gold grade resulting from cooling is ~1 [mg Au/kg quartz] near reservoir conditions, whereas it reaches >10 [mg Au/kg quartz]

Fig. 3. Trace metal content in hydrothermal fluids from Tolhuaca reservoir. Metal content in Lihir Island gold-rich fluids and geothermal fluids from the Taupo Volcanic Zone are shown as reference.

Fig. 5. External and internal triggers for gold precipitation. (A) Seismically-triggered and internally-forced fluid pathways in *P–H* space. The red curves show the calculated gold solubilities in parts per billion (ppb) within the single-phase and two-phase ($L + V$, light blue) fields. The blue arrow shows the adiabatic pressure drop from metastable reservoir conditions (orange circle) to lower pressures (blue/white circles), triggered by a suction pump-like mechanism for different earthquake magnitudes (Mw). Shaded in yellow is the optimal range for gold precipitation triggered by adiabatic pressure decrease ($P \sim P_{sat}$ and $P < 150$ bar).

for small adiabatic pressure drops (≤10 bar) at pressures bellow 100 bar. The increase of gold–quartz mass ratio at pressures higher than 150 bar for the adiabatic pressure drop paths is caused by the retrograde quartz solubility and does not represent an increase in the gold precipitation efficiency.

4.3. Transient pressure drop driven by the suction pump mechanism

The suction pump piston model was used to evaluate the effects of co-seismic changes on the thermodynamic conditions of hydrothermal fluids in the epithermal environment. The transient pressure drop that occurs within a dilational jog produced by fault rupture during earthquakes is shown in Fig. 5. Under the estimated reservoir conditions at Tolhuaca ($T_{sat} \sim 300$ °C, $P_{sat} \sim 85$ bar), our calculations indicate that a pressure drop of 54 bar, equivalent to a seismic event of Mw = 2, would generate a mass vapor fraction of 0.18 and at least a 2 log-units decrease in gold solubility (Figs. 5 and 6A). Calculations for variable pre-seismic initial conditions (pressure and enthalpy) within the liquid-saturated curve are shown in Fig. 6A.

5. Discussions

5.1. Optimal window for gold precipitation

The combination of fluid chemistry data and thermodynamic modeling at Tolhuaca indicates that gold solubility is critically affected by *P–T–H* trajectories followed by the precious metal-rich carrier fluid. The trace metal content of fluids in the Tolhuaca geothermal reservoir are broadly similar to those measured in geothermal systems in the Taupo Volcanic Zone (New Zealand) and in the active Lihir hydrothermal gold deposit (Papua New Guinea), supporting the use of Tolhuaca as an analogue of

the epithermal environment (Fig. 3). Measured gold content of fluid at Tolhuaca (1.6 ppb) is within the range of gold solubility calculated at reservoir conditions (1–2 ppb; Fig. 5).

Although gold solubility calculation is dependent on fluid chemistry, the topology of the diagrams in Figs. 5 and 6 is not affected by slightly different initial fluid chemistry – including pH and sulfur content – within the range of the low sulfidation epithermal environment conditions and therefore are likely to describe precipitation and transport processes in such environment. Calculated gold solubility is consistent with updated databases and experimental results (Stefánsson and Seward, 2004) as well as with more recent studies of gold behavior in epithermal environments (Williams-Jones et al., 2009). Significantly higher gold concentrations than considered here are possible, if H_2S concentrations are higher, increasing approximately with the square of the H_2S activity, as shown by reactions (1) and (2) (Williams-Jones et al., 2009; Stefánsson and Seward, 2004). Such conditions can be met if low-salinity magmatic fluids are injected into the base of the convective geothermal system. In this scenario, the same triggers for gold precipitation will apply but efficiency will increase. Magmatic fluid input may thus explain the temporarily much higher gold contents reported in fluid inclusions from epithermal gold deposits (up to 3000 ppb; Márquez-Zavalía and Heinrich, 2016) compared to active geothermal systems. Higher Au and S concentrations also imply that higher-grade deposits may form in a correspondingly shorter time (Heinrich, 2005; Heinrich, 2006; Simmons & Brown, 2006; Márquez-Zavalía and Heinrich, 2016).

Our calculations show high solubility conditions for gold in the liquid-phase region between ~210 and 370 °C ($P_{sat} = 20$ to 220 bar; Fig. 5), as widely recognized for epithermal environments (e.g., Simmons et al., 2005; Williams-Jones et al., 2009). More interestingly, gold solubility calculations in *P–H* space indicate that the effect of small pressure changes on gold solubility is enhanced at specific thermodynamic conditions (Fig. 5). Therefore, we recognize an optimal window for efficient gold precipitation that can be triggered by relatively subtle adiabatic pressure drops. Such window is at liquid-saturated conditions (boiling), relatively high temperatures (210 °C < T_{sat} < 310 °C) and corresponding saturated liquid pressures (20 bar < P_{sat} < 100 bar), coincident with the documented ore precipitation conditions in epithermal gold deposits (Simmons et al., 2005) (Fig. 5). Such optimal conditions at the two-phase boundary are developed through a combination of sustained heat and high permeability conditions, as previous studies have shown (e.g. Hayba and Ingebritsen, 1997; Weis et al., 2012), and can be sustained at the geothermal reservoir until the waning and cooling of the hydrothermal system.

Our gold solubility results in Fig. 6A show that precipitation efficiency of relatively small adiabatic pressure drops (20 bar) at reservoir conditions of Tolhuaca is high (70%) and for an equivalent efficiency would alternatively require a significant cooling (>120 °C). Furthermore, the gold-quartz mass ratio of up to 30 g Au/t resulting from an adiabatic pressure drop within the optimal window – represented by a red vertical arrow in Fig. 6A and D – is consistent with observed gold grades in small tonnage, high-grade orebodies (10–100 g Au/t, Simmons et al., 2005). In turn, isobaric cooling pathways – represented by a green horizontal arrow in Fig. 6A and D – result in gold grades of <5 g Au/t, similar to those described in large tonnage, low-grade orebodies (1–2 g Au/t, Simmons et al., 2005). These results support the idea invoked in petrographic and mineralogical studies of ore textures and fluid inclusion assemblages that flash vaporization is more efficient than gentle boiling for ore precipitation (Moncada et al., 2012).

The estimated pressure drops driven by earthquakes through the suction pump mechanism indicate that even small magnitude earthquakes (Mw < 2) can trigger efficient gold precipitation if the system is initially at the optimal conditions for gold precipitation (Figs. 5 & 6). This result is relevant since previous studies have proposed that
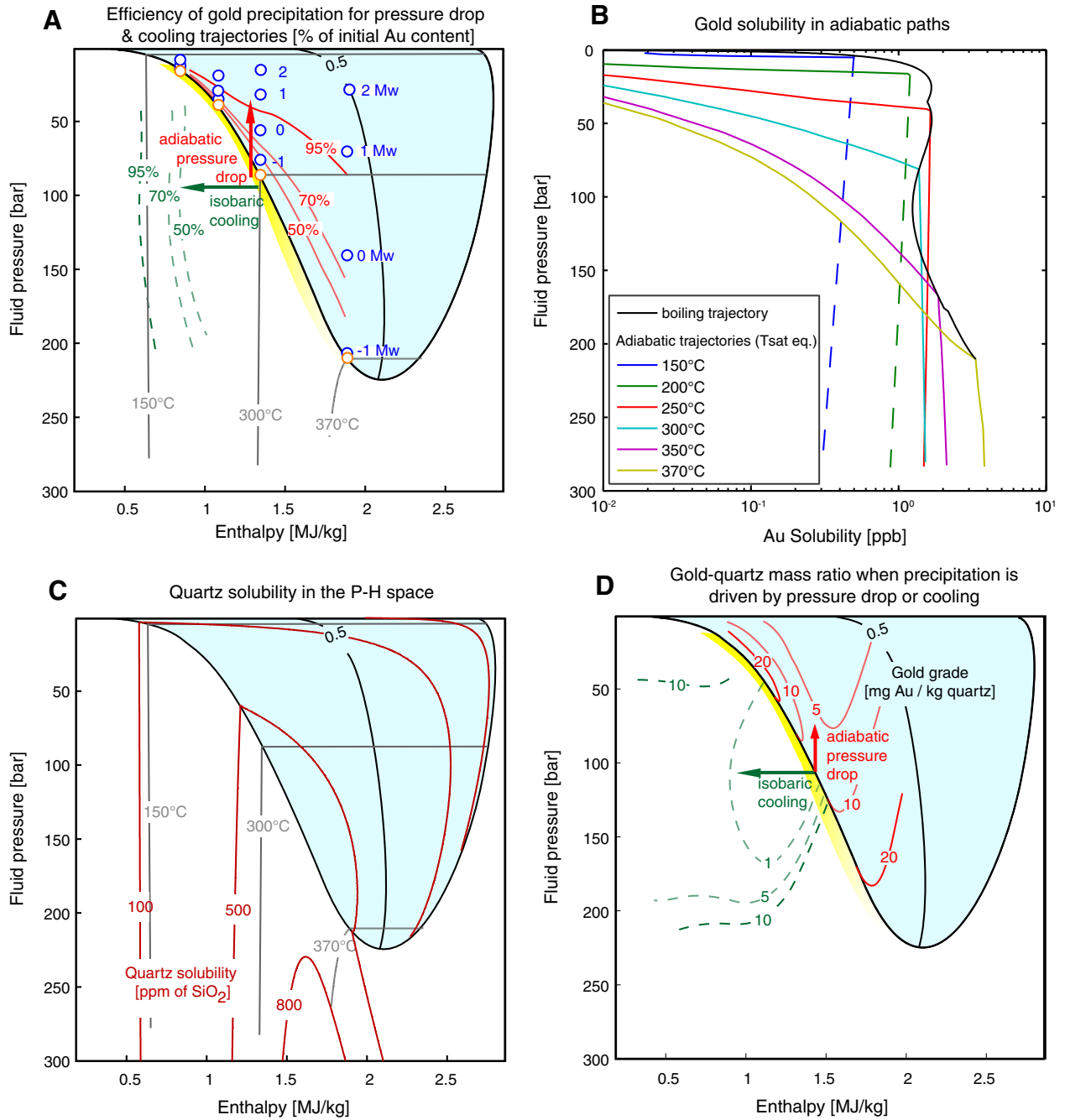
Fig. 6. Gold precipitation efficiency in pressure–enthalpy space. (A) Gold precipitation efficiency (%) driven by adiabatic pressure drop (red arrow and solid red curves) and (ii) isobaric cooling (green arrow and dashed green curves), considering liquid saturated conditions as a starting point. Transient fluid pressures (blue circles) triggered by a suction pump mechanism for different earthquake magnitudes (Mw) and different starting temperatures (200, 250, 300 and 370 °C; orange circles) are shown for reference. Adiabatic pressure drops have the highest efficiencies at $P_{sat} < 100$ bar, whereas isobaric cooling requires a significant temperature decrease ($\Delta T \sim 150$ °C) to precipitate most of the dissolved gold. (B) Gold solubility along six adiabatic paths (colored curves) and under boiling conditions (black curve). The enthalpy of the fluid was converted to the equivalent temperature at saturated liquid conditions. (C) Quartz solubility in *P–H* space depicting its prograde ($150 < T < 350$ °C) and retrograde ($T > 350$ °C) behavior. Quartz thermodynamic data is from Manning (1994) (D) Gold-quartz mass ratio resulting from precipitation driven by adiabatic pressure drop and isobaric cooling. The calculated gold–quartz mass ratio represents the gold grade in an idealized quartz vein. Results are consistent with reported data of gold content in gold-rich (>10 ppm Au) and gold-poor (<1 ppm Au) quartz veins (Sillitoe and Hedenquist, 2003; Simmons et al., 2005).

changes in physical parameters such as permeability and/or pressure triggered by fault rupture lead to efficient precipitation of gold in hydrothermal systems at any initial condition (e.g., Micklethwaite et al., 2015). Therefore, our results strongly suggest that ore fluids feeding the hydrothermal reservoir must evolve towards optimal conditions (20 bar < P_{sat} < 100 bar; 210 °C < T_{sat} < 310 °C) before – or concomitantly with – the occurrence of a seismic event, so that gold solubility is efficiently reduced through flash vaporization.

6. Further implications

Since our results reveal that gold solubility is significantly affected by subtle adiabatic pressure releases (e.g., ~10 bar) triggered by earthquakes, the key question is how seismic activity transiently promotes gold precipitation and enhances the ore forming process. In this section we explore the long-term contribution of earthquake-triggered precipitation to epithermal gold deposit formation by considering the suction

pump mechanism. In this particular case, the time-integrated contribution can be estimated after calculating the mass of vaporized fluid, the initial gold content of the fluid and the earthquake frequency. The mass of vaporized fluid is directly related to the volume change within the dilational jog. This volume change is independent of the initial effective aperture thickness of the dilational jog 'd'. We assume that even small earthquakes (Mw > 0) trigger the vaporization of most of the fluid within dilational jogs and the precipitation of the gold (and quartz) dissolved in hydrothermal fluid, based on previous works (Sibson, 1987; Weatherley and Henley, 2013) and the results presented in Section 4.1. Considering that the system flashes (boils adiabatically) until the pre-seismic pressure is reached via new fluid inflow, it is reasonable to assume that the volume of vaporized fluid by the suction pump mechanism can be estimated as the co-seismic volume increase (ΔV). Therefore, in each seismic event, the amount of precipitated gold is equal to the mass of metal contained in the volume of vaporized fluid – equivalent to the co-seismic volume increase (ΔV) – which is dependent on the magnitude of the earthquake:

$$Au_{EQ} = m_{Au\_liquid}\rho\Delta V_{EQ} \tag{7}$$

The gold precipitated in a given earthquake magnitude range results from the multiplication of the gold precipitated (Au_{EQ} in moles) by the number of earthquakes occurring in a specific time-span (e.g., 1 ka). Then, the long-term effect is the integrated contribution of earthquakes of variable magnitude, as described in Eq. (8):

$$Au_{total} = m_{Au\_liquid}\rho\int_{Mw=-2}^{Mw=8}\Delta V_{EQ}N_{EQ}dMw \tag{8}$$

where N is the number of earthquakes within a magnitude range dMw per time-unit.

As earthquake frequency (incremental magnitude–frequency distribution) is scale-dependent we assume that the spatial extension of active geothermal systems is the reasonable scale to represent the epithermal environment. Due to the lack of adequate seismic records at the local scale for the greenfields of Tolhuaca, we used the earthquake density distribution data from the Liquiñe–Ofqui Fault System in its southern termination (Lange et al., 2008) as an estimation of the frequency of tectonic-induced earthquakes in the area.

Since seismicity and the amount of dissolved gold in the ore fluids are key variables that may affect the time-integrated contribution to gold precipitation in epithermal systems, we analyze their effect on gold precipitation rates. As a first order approximation, we integrate the amount of gold precipitated over time for different earthquake density distributions and variable gold concentrations in the fluid. Different earthquake density distributions were synthetically constructed by increasing and decreasing the earthquake frequency for a constant b-value of 1, which is typical for tectonically-induced events and depends inversely on differential stress (Schorlemmer et al., 2005). Fluid-induced earthquake swarms, on the other hand, have higher b-values that can be as large as 2.5 (Legrand et al., 2011).

Considering that the magnitude of an earthquake is directly related to the length of the co-seismic slip and the volume within dilational jogs, it is clear that the vaporized mass of the ore-forming fluid grow exponentially with increasing earthquake magnitude (Fig. 7A) (Weatherley and Henley, 2013). On the other hand, large-magnitude earthquakes are significantly less frequent than small-magnitude earthquakes, as shown by the Gutenberg–Richter relationship in Fig. 7B. Therefore, the amount of fluid affected by seismically-triggered flash vaporization over a certain period of time (Fig. 7C) will depend on these two counteracting effects, i.e., minor earthquakes trigger precipitation of smaller amounts of gold relatively frequently, whereas infrequent major earthquakes affect large volumes of hydrothermal fluids and thus have the potential to precipitate very large quantities of gold.

The time-integrated contribution of earthquake-triggered precipitation shown in Fig. 7C was calculated taking into account the gold content of the fluid in Tolhuaca (~1 ppb), and an earthquake magnitude relationship for the LOFS (Lange et al., 2008) defined by a b-value ~1 for a 1000 year period. The area below the curve in Fig. 7C represents the total mass of gold precipitated per ka, and reveals that earthquakes with magnitude between 4 Mw and 7 Mw contribute ~70% of the total gold precipitated in a hydrothermal reservoir undergoing seismic activity. The association of gold precipitation to low and intermediate-magnitude earthquakes, i.e., small and intermediate slips (4 Mw: 3 cm–7 Mw: 1.1 m), is consistent with the observation that, second-order fractures are predominant in high-grade Au veins in geothermal systems and epithermal gold deposits (Simmons et al., 2005).

According to our calculations, the earthquake-enhanced gold precipitation rate at Tolhuaca is small (0.5 kg/ka), requiring ~58 Ma to build up a 1 Moz (~31.1 t) Au ore body (Fig. 7C). When this rate is calculated for different earthquake density distributions and variable gold concentrations for the sake of comparison, results show that the gold precipitation rate at Tolhuaca (orange box in Fig. 8) would increase by two orders of magnitude if fluids had a gold budget as large as those from, e.g., Lihir Island gold-rich fluids (vertical segmented line, Fig. 8). These calculations also indicate that a 10-fold increase in seismicity produces a 10-fold increase in gold precipitation rate for a given gold content in the fluid.
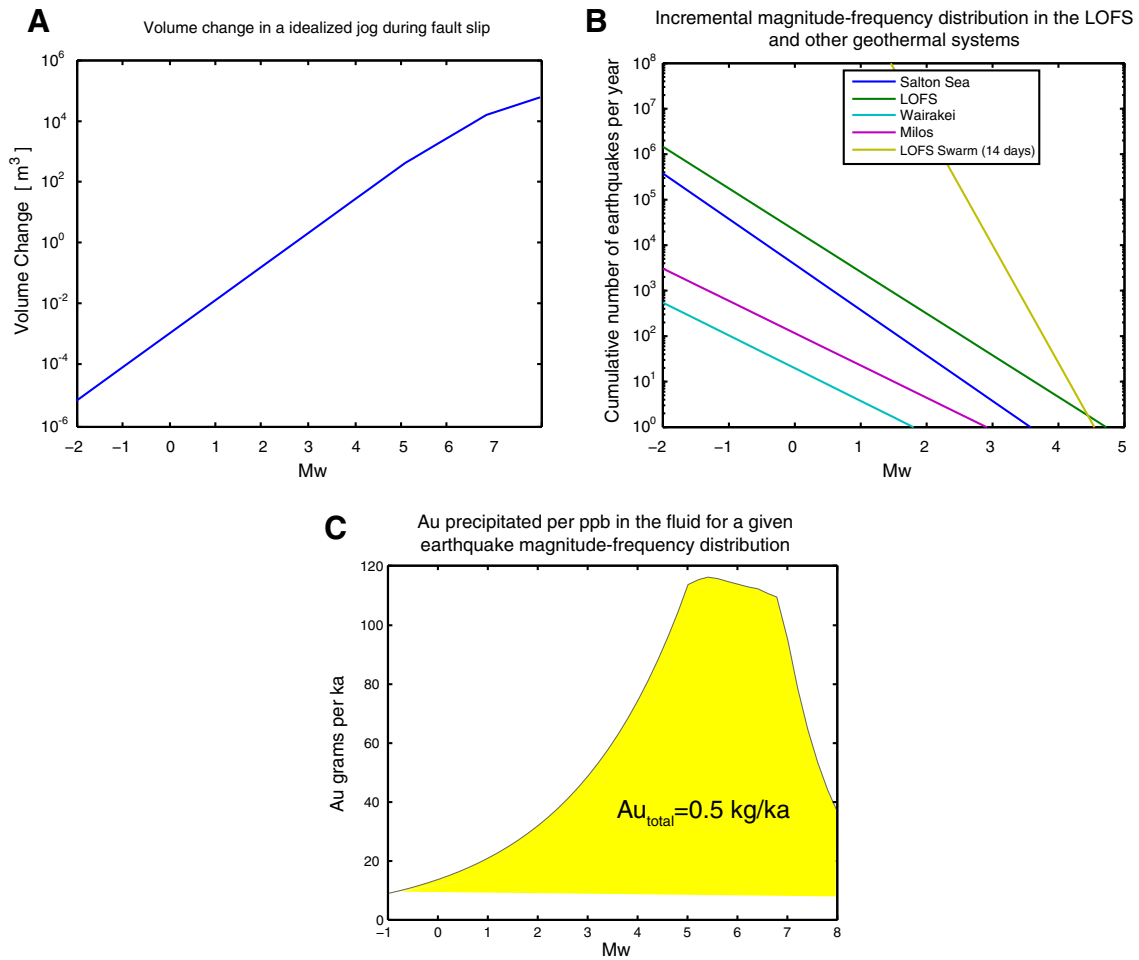
The calculated rates of gold precipitation enhanced by seismic activity in Fig. 8, allow a first order comparison with gross estimations on the gold precipitation rates in epithermal deposits. We selected the Hauraki Goldfield (New Zealand) and the Hishikari (Japan) low-sulfidation epithermal deposits because they represent similar conditions than those at Tolhuaca. In these deposits mineralization is concentrated in veins, associated to low salinity hydrothermal fluids (<1.8dd wt.% NaCl equiv.) and related to extensional or mildly extensional tectonic settings (Izawa et al., 1990; Mauk et al., 2011). The Waihi gold deposit hosts 167 t of gold (Brathwaite and Faure, 2002) and available data indicate that most of the known gold endowment was deposited in a 390 to 460 ka window (Mauk et al., 2011). The Hishikari epithermal deposit contains c.a. 260 t of gold (Izawa et al., 1990) and $^{40}Ar/^{39}Ar$ dating of adularia indicate that the deposit was formed in <260 ka (Sanematsu et al., 2006). Therefore, a gross rate of tonnes of gold precipitated per 1000 years (t/ka) are estimated in 0.43 t/ka for Waihi and 1 t/ka for Hishikari gold deposits. In comparison with Tolhuaca (0.0005 t of gold precipitated per ka), these broad estimations are two to four orders of magnitude higher. These higher gold precipitation rates, which are still minimum rates considering the precision of geochronological estimate, place Waihi and Hishikari deposits in the upper right region of Fig. 8, showing that higher gold content in the fluid and/or increased seismicity would be required to build a large epithermal gold deposit in the Tolhuaca system.

Although the actual rates in natural systems are very likely affected by other variables (e.g., changes in hydrology, stress regime, magmatic activity and compositional variations of the fluids, among many others), these results are a first step towards quantifying the effects of long-term seismicity on ore precipitation, and should motivate further and more detailed studies.

7. Concluding remarks

This study integrates geochemical and structural data from the active Tolhuaca geothermal system in southern Chile to understand the interplay between seismic activity, fluid flow and gold precipitation in the epithermal environment. By combining borehole and fluid chemistry data with thermodynamic modeling we conclude that the efficiency of gold precipitation is highly dependent on the P–T–H initial conditions of the high-enthalpy hydrothermal reservoir, and become optimal at liquid-saturated conditions and pressures below 100 bar (210 °C < T_{sat} < 310 °C). Our key result indicates that under such P–T conditions, very efficient gold extraction from hydrothermal solutions can be achieved by pressure drop and associated phase separation.

A

Volume change in a idealized jog during fault slip

B

Incremental magnitude-frequency distribution in the LOFS and other geothermal systems

C

Au precipitated per ppb in the fluid for a given earthquake magnitude-frequency distribution

Au_{total}=0.5 kg/ka

Fig. 7. Time-integrated contribution of earthquakes to gold precipitation rates. (A) Co-seismic volume increase in a jog for different earthquake magnitudes (Mw). Calculations are based on Weatherley and Henley (2013). (B) Incremental magnitude–frequency distribution in the LOFS, Chile (Lange et al., 2008). Seismicity in Salton Sea, Milos and Wairakei (WK) geothermal systems are shown as a reference. (C) Time-integrated contribution of earthquake-triggered precipitation to gold deposit formation in a time span of 1 ka, for a fluid containing 1 ppb of gold using LOFS incremental magnitude–frequency distribution as reference for calculation.

These calculated conditions are coincident with the documented ore precipitation conditions described in epithermal gold deposits.
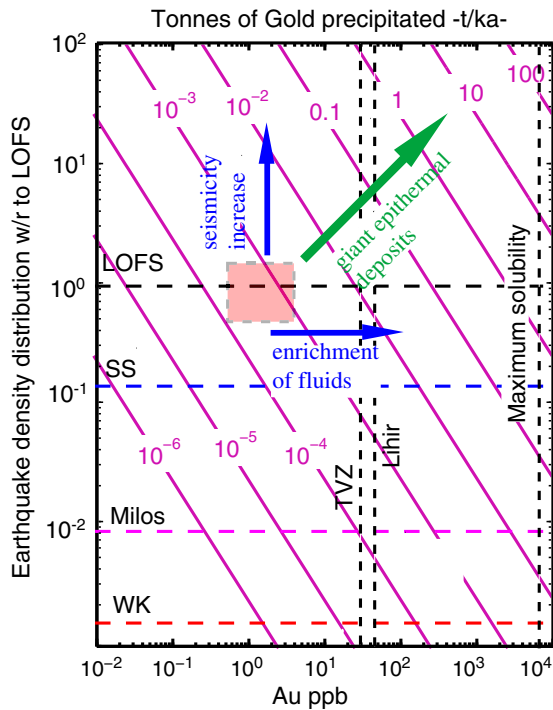
This optimal environment develops through a combination of sustained heat and high permeability conditions, and can be perturbed by subtle adiabatic pressure decreases (~5–20 bar). When the suction pump piston model is used to evaluate the effects of co-seismic changes on the thermodynamic conditions of hydrothermal fluids, the transient pressure drop that occurs within dilational jog produced by fault rupture during earthquakes (e.g., Mw = 2) would generate a pressure drop of ~55 bar, a vapor fraction of ~0.20 and at least a 2 log-unit decrease in gold solubility. These results indicate that even small magnitude earthquakes (Mw < 2) can efficiently trigger gold precipitation if the system is initially at the optimal conditions. Furthermore, we show that, although gentle boiling drives some gold deposition, flash vaporization occurring under these optimal window conditions maximizes the extraction of gold from the ore fluid.

The results presented in this study are in close agreement with the notion that gold precipitation in the shallower portions of hydrothermal systems is modulated by a sustained supply of metals from a magmatic–hydrothermal source, an efficient ore transport mechanism that ensures high gold-solubility conditions, followed by chemical changes or physical perturbations of a hydrothermal reservoir. Such conditions result from an ideal interplay between seismic activity, fluid flow, transient solubility changes and P–T–H fluctuations that may significantly enhance gold precipitation rates in the shallow crust and lead to overall increases in metal endowment over time.

Fig. 8. Gold precipitation rates triggered by the suction pump mechanism during earthquakes. Gold precipitation rates (magenta diagonal lines, in tonnes (t) per 1000 years (ka)) are plotted as a function of gold content of the fluid (in ppb) and earthquake density distribution relative to the LOFS. The upper limits for gold content in hydrothermal fluids from geothermal systems and epithermal gold deposits are shown as vertical segmented lines for comparison Seismicity at Salton Sea (SS), Milos and Wairakei (WK) geothermal systems are shown for reference. The light-red shaded region constrains the window of seismicity vs. gold precipitation at Tolhuaca. Taupo Volcanic Zone, Lihir and maximum solubility data were taken from Simmons and Brown (2006, 2007) and Hurtig and Williams-Jones (2014).

References

Arnórsson, S., Sigurdsson, S., Svavarsson, H., 1982. The chemistry of geothermal waters in Iceland. I. Calculation of aqueous speciation from 0 °C to 370 °C. Geochim. Cosmochim. Acta 46, 1513–1532.

Brathwaite, R.L., Faure, K., 2002. The Waihi epithermal gold-silver-base metal sulfide-quartz vein system, New Zealand: Temperature and salinity controls on electrum and sulfide deposition. Econ. Geol. 97 (2), 269–290. http://dx.doi.org/10.2113/gsecongeo.97.2.269.

Cembrano, J., Lara, L., 2009. The link between volcanism and tectonics in the southern volcanic zone of the Chilean Andes: a review. Tectonophysics 471, 96–113. http://dx.doi.org/10.1016/j.tecto.2009.02.038.

Curewitz, D., Karson, J.A., 1997. Structural settings of hydrothermal outflow: fracture permeability maintained by fault propagation and interaction. J. Volcanol. Geotherm. Res. 79, 149–168. http://dx.doi.org/10.1016/S0377-0273(97)00027-9.

Hayba, D.O., Ingebritsen, S.E., 1997. Multiphase groundwater flow near cooling plutons. J. Geophys. Res. 102, 12235. http://dx.doi.org/10.1029/97JB00552.

Heinrich, C.A., 2005. The physical and chemical evolution of low-salinity magmatic fluids at the porphyry to epithermal transition: a thermodynamic study. Mineral. Deposita 39, 864–889. http://dx.doi.org/10.1007/s00126-004-0461-9.

Heinrich, C.A., 2006. Geochemistry. How fast does gold trickle out of volcanoes? Science (New York, N.Y.) 314 (5797), 263–264. http://dx.doi.org/10.1126/science.1134456.

Henley, R., Hughes, G., 2000. Underground fumaroles: "excess heat" effects in vein formation. Econ. Geol. 95, 453–466.

Holmgren, M., 2007. XSteam: Water and Steam Properties According to IAPWS IF-97.

Hummel, W., Berner, U., Curti, E., Pearson, F.J., Thoenen, T., 2002. Nagra/PSI chemical thermodynamic data base 01/01. Nagra NTB 02-16, Nagra, Wettingen, Switzerland.

Hurtig, N.C., Williams-Jones, A.E., 2014. An experimental study of the transport of gold through hydration of AuCl in aqueous vapour and vapour-like fluids. Geochim. Cosmochim. Acta 127, 305–325. http://dx.doi.org/10.1016/j.gca.2013.11.029.

Izawa, E., Urashima, Y., Ibaraki, K., Suzuki, R., Yokoyama, T., Kawasaki, K., Koga, A., Taguchi, S., 1990. The Hishikari gold deposit: high-grade epithermal veins in Quaternary volcanics of southern Kyushu, Japan. J. Geochem. Explor. 36, 1–56.

Johnson, J.W., Oelkers, E.H., Helgeson, H.C., 1992. SUPCRT92: a software package for calculating the standard molal thermodynamic properties of minerals, gases, aqueous

species, and reactions from 1 to 5000 bar and 0 to 1000 °C. Comput. Geosci. 18, 899–947. http://dx.doi.org/10.1016/0098-3004(92)90029-Q.

Kulik, D.a., Wagner, T., Dmytrieva, S.V., Kosakowski, G., Hingerl, F.F., Chudnenko, K.V., Berner, U.R., 2012. GEM-Selektor geochemical modeling package: revised algorithm and GEMS3K numerical kernel for coupled simulation codes. Comput. Geosci. 1–24. http://dx.doi.org/10.1007/s10596-012-9310-6.

Lange, D., Cembrano, J., Rietbrock, A., Haberland, C., Dahm, T., Bataille, K., 2008. First seismic record for intra-arc strike-slip tectonics along the Liquiñe–Ofqui fault zone at the obliquely convergent plate margin of the southern Andes. Tectonophysics 455, 14–24. http://dx.doi.org/10.1016/j.tecto.2008.04.014.

Legrand, D., Barrientos, S., Bataille, K., Cembrano, J., Pavez, a., 2011. The fluid-driven tectonic swarm of Aysen Fjord, Chile (2007) associated with two earthquakes (Mw = 6.1 and Mw = 6.2) within the Liquiñe–Ofqui fault zone. Cont. Shelf Res. 31, 154–161. http://dx.doi.org/10.1016/j.csr.2010.05.008.

Leonard, M., 2010. Earthquake fault scaling: self-consistent relating of rupture length, width, average displacement, and moment release. Bull. Seismol. Soc. Am. 100, 1971–1988. http://dx.doi.org/10.1785/0120090189.

Leonard, M., 2014. Self-consistent earthquake fault-scaling relations: update and extension to stable continental strike-slip faults. Bull. Seismol. Soc. Am. 104, 2953–2965. http://dx.doi.org/10.1785/0120140087.

Manning, C.E., 1994. The solubility of quartz in H_2O in the lower crust and upper mantle. Geochim. Cosmochim. Acta 58, 4831–4839. http://dx.doi.org/10.1016/0016-7037(94)90214-3.

Márquez-Zavalía, M.F., Heinrich, C.A., 2016. Fluid evolution in a volcanic-hosted epithermal carbonate–base metal–gold vein system: Alto de la Blenda, Farallón Negro, Argentina. Mineral. Deposita http://dx.doi.org/10.1007/s00126-016-0639-y.

Mauk, J.L., Hall, C.M., Chesley, J.T., Barra, F., 2011. Punctuated evolution of a large epithermal province: the Hauraki goldfield, New Zealand. Econ. Geol. 106 (6), 921–943. http://dx.doi.org/10.2113/econgeo.106.6.921.

Melosh, G., Moore, J., Stacey, R., 2012. Natural Reservoir Evolution in the Tolhuaca Geothermal Field, Southern Chile. 37th Workshop on Geothermal Reservoir Engineering Stanford University, Stanford, California, January 31–February 1, 2012 (SGP-TR-194).

Micklethwaite, S., Ford, a., Witt, W., Sheldon, H.a., 2015. The where and how of faults, fluids and permeability — insights from fault stepovers, scaling properties and gold mineralisation. Geofluids 15, 240–251. http://dx.doi.org/10.1111/gfl.12102.

Moncada, D., Mutchler, S., Nieto, a., Reynolds, T.J., Rimstidt, J.D., Bodnar, R.J., 2012. Mineral textures and fluid inclusion petrography of the epithermal Ag–Au deposits at Guanajuato, Mexico: application to exploration. J. Geochem. Explor. 114, 20–35. http://dx.doi.org/10.1016/j.gexplo.2011.12.001.

Perez-Flores, P., Cembrano, J., Sanchez, P., Veloso, E., Arancibia, G., Roquer, T., 2016. Tectonics, magmatism and paleo-fluid distribution in a strike-slip setting: insights from the northern termination of the Liquiñe–Ofqui Fault System, Chile. Tectonophysics 680, 192–210. http://dx.doi.org/10.1016/j.tecto.2016.05.016.

Richards, J.P., 2013. Giant ore deposits formed by optimal alignments and combinations of geological processes. Nat. Geosci. 6, 911–916. http://dx.doi.org/10.1038/ngeo1920.

Rowland, J.V., Simmons, S.F., 2012. Hydrologic, magmatic, and tectonic controls on hydrothermal flow, Taupo volcanic zone, New Zealand: implications for the formation of epithermal vein deposits. Econ. Geol. 107, 427–457. http://dx.doi.org/10.2113/econgeo.107.3.427.

Sánchez, P., Pérez-Flores, P., Arancibia, G., Cembrano, J., Reich, M., 2013. Crustal deformation effects on the chemical evolution of geothermal systems: the intra-arc Liquiñe–Ofqui Fault System, Southern Andes. Int. Geol. Rev. 55, 1384–1400. http://dx.doi.org/10.1080/00206814.2013.775731.

Sanchez-Alfaro, P., Reich, M., Arancibia, G., Pérez-Flores, P., Cembrano, J., Driesner, T., Lizama, M., Rowland, J., Morata, D., Heinrich, C.A., Tardani, D., Campos, E., 2016. Physical, chemical and mineralogical evolution of the Tolhuaca geothermal system, southern Andes, Chile: insights into the interplay between hydrothermal alteration and brittle deformation. J. Volcanol. Geotherm. Res. http://dx.doi.org/10.1016/j.jvolgeores.2016.05.009.

Sanematsu, K., Watanabe, K., Duncan, R.A., Izawa, E., 2006. The history of vein formation determined by 40Ar/39AR dating of adularia in the Hosen-1 vein at the Hishikari epithermal gold deposit, Japan. Econ. Geol. 101 (3), 685–698. http://dx.doi.org/10.2113/gsecongeo.101.3.685.

Schorlemmer, D., Wiemer, S., Wyss, M., 2005. Variations in earthquake-size distribution across different stress regimes. Nature 437, 539–542. http://dx.doi.org/10.1038/nature04094.

Scott, S., Gunnarsson, I., Arnórsson, S., Stefánsson, A., 2014. Gas chemistry, boiling and phase segregation in a geothermal system, Hellisheidi, Iceland. Geochim. Cosmochim. Acta 124, 170–189. http://dx.doi.org/10.1016/j.gca.2013.09.027.

Sibson, R., Scott, J., 1998. Stress/fault controls on the containment and release of overpressured fluids: examples from gold–quartz vein systems in Juneau, Alaska; Victoria, Australia and Otago, New Zealand. Ore Geol. Rev. 13, 293–306. http://dx.doi.org/10.1016/S0169-1368(97)00023-1.

Sibson, R.H., 1987. Earthquake rupturing as a mineralizing agent in hydrothermal systems. Geology 15, 701. http://dx.doi.org/10.1130/0091-7613(1987)15<701:ERAAMA>2.0.CO;2.

Sibson, R.H., 2003. Brittle-failure controls on maximum sustainable overpressure in different tectonic regimes. Am. Assoc. Pet. Geol. Bull. 87, 901–908. http://dx.doi.org/10.1306/01290300181.

Sibson, R.H., Robert, F., Poulsen, K.H., 1988. High-angle reverse faults, fluid-pressure cycling, and mesothermal gold-quartz deposits. Geology 16, 551. http://dx.doi.org/10.1130/0091-7613(1988)016<0551:

Sillitoe, R., Hedenquist, J., 2003. Linkages between volcanotectonic settings, ore-fluid compositions, and epithermal precious metal deposits. In: Simmons, S.F., Graham, I. (Eds.), Volcanic, Geothermal and Oreforming Fluids; Rulers and Witnesses of Processes within the Earth. Society of Economic Geologists Special Publication Vol. 10, pp. 315–343.

Simmons, S.F., Brown, K.L., 2006. Gold in magmatic hydrothermal solutions and the rapid formation of a giant ore deposit. Science New York, N.Y. 314 (5797), 288–291. http://dx.doi.org/10.1126/science.1132866.

Simmons, S.F., Brown, K.L., 2007. The flux of gold and related metals through a volcanic arc, Taupo Volcanic Zone, New Zealand. Geology 35 (12), 1099. http://dx.doi.org/10.1130/G24022A.1.

Simmons, S.F., White, N., John, D., 2005. Geological characteristics of epithermal precious and base metal deposits. Econ. Geol. 100th Anni, pp. 485–522.

Stefánsson, A., Seward, T.M., 2003a. The hydrolysis of gold(I) in aqueous solutions to 600 °C and 1500 bar. Geochim. Cosmochim. Acta 67, 1677–1688. http://dx.doi.org/10.1016/S0016-7037(02)01131-6.

Stefánsson, A., Seward, T.M., 2003b. Stability of chloridogold(I) complexes in aqueous solutions from 300 to 600 °C and from 500 to 1800 bar. Geochim. Cosmochim. Acta 67, 4559–4576. http://dx.doi.org/10.1016/S0016-7037(03)00391-0.

Stefánsson, A., Seward, T.M., 2004. Gold(I) complexing in aqueous sulphide solutions to 500 °C at 500 bar. Geochim. Cosmochim. Acta 68, 4121–4143. http://dx.doi.org/10.1016/j.gca.2004.04.006.

Tardani, D., Reich, M., Roulleau, E., Takahata, N., Sano, Y., Peréz-Flóres, P., Sanchez-Alfaro, P., Arancibia, G., 2016. Exploring the structural controls on helium, nitrogen and carbon isotope signatures in hydrothermal fluids along an intra-arc fault system. Geochim. Cosmochim. Acta 184, 193–211. http://dx.doi.org/10.1016/j.gca.2016.04.031.

Weatherley, D.K., Henley, R.W., 2013. Flash vaporization during earthquakes evidenced by gold deposits. Nat. Geosci. 6, 294–298. http://dx.doi.org/10.1038/ngeo1759.

Weis, P., Driesner, T., Heinrich, C.A., 2012. Porphyry-copper ore shells form at stable pressure-temperature fronts within dynamic fluid plumes. Science 338, 1613–1616. http://dx.doi.org/10.1126/science.1225009.

Williams-Jones, A.E., Bowell, R.J., Migdisov, a.a., 2009. Gold in solution. Elements 5, 281–287. http://dx.doi.org/10.2113/gselements.5.5.281.